https://doi.org/10.1007/s41230-025-4118-x

Effect of CNT content on microstructure and tribological properties of CNTs/AlSi10Mg composites by LPBF

Li-yi Jiang[1, 2], Chao-yi Shen[1], Ting-ting Liu[2], Chang-dong Zhang[2], Xiang Su[3, 4], Wei-wei Xu[1], Bo-xiang Wang[1], *Zhi-xiang Qi[3], and Wen-he Liao[2]

1. School of Mechanical Engineering, Nanjing Institute of Technology, Nanjing 211167, China

2. National Joint Engineering Research Center of NC forming technology and equipment, School of Mechanical Engineering, Nanjing University of Science and Technology, Nanjing 210094, China

3. Jiangsu Belight Laboratory, State Key Laboratory of Advanced Casting Technologies, Nanjing University of Science and Technology, Nanjing 210094, China

4. School of Aviation and Mechanical Engineering, Changzhou Institute of Technology, Changzhou 213032, Jiangsu, China

Abstract: In this study, carbon nanotubes (CNTs)/AlSi10Mg composite parts with CNTs contents ranging from 0.0 to 2.0wt.% were successfully fabricated via laser powder bed fusion (LPBF) with laser scan speeds ranging from 900 to 1,900 mm·s^{-1}. Uniform dispersion of CNTs in the powders can be achieved when their content is below 2.0wt.%. In the LPBF samples, the morphology of the CNTs is found to be directly related to their content. Especially, the length of CNTs in samples prepared by LPBF increases as the CNT content increases. The length of CNTs is approximately 200–300 nm in the 1.0wt.% CNTs/AlSi10Mg composites and approximately 500–1,000 nm in the 2.0wt.% CNTs/AlSi10Mg composites. The hardness of the composites reaches its highest value of 143.3 HV when the CNTs content is 1.0wt.% and the laser scan speed is 1,300 mm·s^{-1}. It is found that the self-lubricating properties of the CNTs improve the tribological properties of the composites. The coefficient of friction (CoF) and wear rate of the samples decrease with increasing CNT content. At a CNTs content of 2.0wt.%, the CoF and wear rate of the composite decrease by approximately 14% and 30%, respectively, compared to the unreinforced matrix. The presence of CNTs leads to a more complete and refined network microstructure within the samples. Both the CNTs and the aluminum carbide contribute to the Orowan mechanism and the Hall-Petch effect within the matrix.

Keywords: carbon nanotubes (CNTs); aluminum matrix composites; laser powder bed fusion (LPBF); hardness; coefficient of friction (CoF)

CLC numbers: TG146.21 **Document code:** A **Article ID:** 1672-6421(2025)04-439-10

1 Introduction

Aluminum alloys are widely favored for aerospace and automotive applications due to their high specific strength. Among the various types of aluminum alloys, cast aluminum alloys are commonly used in engine components, where tribological performance is critical. However, cast aluminum alloys with limited wear resistance may not withstand the loads required for more demanding application environments [1, 2]. Incorporating high-performance particles or fibers to aluminum alloys can significantly enhance the wear resistance of the matrix. Research indicates that uniformly dispersed reinforcements within the aluminum matrix can effectively reduce wear loss [3, 4]. Numerous efforts, often involving complex processes, have been made to achieve an optimal distribution of these reinforcements [5-7].

Laser powder bed fusion (LPBF) is one of the most prominent additive manufacturing (AM) technologies, utilizing a laser to selectively melt spread powder to fabricate complex structures based on computer-aided design (CAD) data files [8]. Due to its advantageous

***Zhi-xiang Qi**

Male, born in 1991, Ph. D., Professor, and Doctoral Supervisor. Prof. Qi is the Vice Director of the State Key Laboratory of Advanced Casting Technologies. His research interests mainly focus on the directional solidification and intermetallic high-temperature material technology.

E-mail: zxqi@njust.edu.cn

Received: 2024-05-31; Revised: 2024-12-05; Accepted: 2025-01-22

solidification process, reinforcement can be controlled by melt pool convection at the microscale to achieve significant strengthening, showing great potential in the preparation of metal matrix composites. Yu et al. [9] reviewed the LPBF processing of particle-reinforced metal matrix nanocomposites and highlighted that AlSi10Mg alloys are more suitable as the composite matrix in the LPBF process compared to other aluminum alloys, due to their narrow solidification range. Jue and Gu [10] found that a smaller grain size of cellular dendritic Al matrix could be achieved in LPBF-fabricated aluminum oxide reinforced AlSi10Mg composites, leading to impressive improvements in hardness and tribological properties. When micro aluminum oxide with a content of 2.0wt.% was added, the lowest CoF of 0.3 was achieved under optimal LPBF parameters. Gao et al. [11] utilized nano-TiN to reinforce AlSi10Mg at a content of 2.0wt.%, increasing the microhardness of the composite to 145±4.9 HV. Furthermore, the CoF and wear rate were reduced to 0.43 and $(1.4\pm0.23)\times10^{-3}$ $mm^3 \cdot Nm^{-1}$, respectively. These studies indicate that the tribological properties of aluminum matrix composites fabricated by LPBF can be effectively improved with the addition of reinforcements. However, current research primarily focuses on zero-dimensional particle reinforcements, with relatively fewer studies exploring higher-dimensional reinforcements.

Carbon nanotubes, as a novel one-dimensional reinforcement, have demonstrated significant potential in enhancing and expanding the mechanical, physical, and tribological properties of metal matrix through conventional processes [12]. Recently, LPBF, as a prominent manufacturing process, has garnered significant attention from researchers for the investigation of CNT-reinforced aluminum composites. Among these studies, CNTs have also shown promising results in improving the mechanical properties of Al matrix composites. Zhao et al. [13] investigated the microstructure and properties of 1.0wt.% CNTs/AlSi10Mg composites fabricated by LPBF. They discovered that the introduction of CNTs improved hardness and electrical conductivity, although it increased porosity and resulted in a microstructure similar to that of LPBFed AlSi10Mg. Du et al. [14] compared 0.5wt.% CNTs/AlSi10Mg composites prepared by LPBF and friction stir processing, respectively. Their findings indicated that both techniques were capable of fabricating components with very fine grains, whereas samples fabricated by LPBF exhibited better mechanical properties. In a study by Wang et al. [15] focusing on 1.0wt.% CNTs/AlSi10Mg fabricated by LPBF, a better hardness and tensile strength than AlSi10Mg fabricated by LPBF were observed, reaching up to 143.7 HV and 412±35 MPa, respectively. The enhancements were attributed to grain refinement and dislocation pinning as the strengthening mechanisms. Gu et al. [16] optimized the LPBF processing parameters of laser power of 350 W and scan speed of 2.0 $m \cdot s^{-1}$ on 0.5wt.% CNTs/AlSi10Mg nanocomposites. The fully dense sample was achieved which exhibited high microhardness of 154.12 HV and tensile strength of 420.8 MPa. Jiang et al. [17] investigated the LPBF process for fabricating 1.0wt.% CNTs/AlSi10Mg composites. A significant improvement in hardness and tensile strength was achieved. It was approximately 10% and 20%, respectively, compared to AlSi10Mg. The findings suggest that CNTs could notable enhance mechanical properties of the composites fabricated by LPBF. However, the tribological properties of CNTs/AlSi10Mg composites prepared by LPBF have yet to be reported.

In this study, the tribological properties of CNT-reinforced AlSi10Mg nanocomposites with varying CNT contents fabricated via LPBF were investigated. A colloidal mixing method was employed to achieve uniform distribution of CNTs in the composite powders. The microstructure, mechanical, and friction properties of the LPBF samples were characterized. Additionally, the relationship among these results were discussed.

2 Experiment

2.1 Materials

The CNTs [Fig. 1(a)], with an outer diameter of 20–30 nm, a length of 10–30 μm, and a purity exceeding 98%, were provided by Chengdu Organic Chemistry Co., Ltd. The AlSi10Mg powder [Fig. 1(b)] was supplied by Concept Laser GmbH Co., Ltd. According to the work of Azar and Pourfath [18], N-methyl pyrrolidone (NMP) demonstrated excellent performance in dispersing nanocarbons. To ensure the preservation of sphericity and size distribution of the composite powders, as well as the structural integrity of the CNTs, a colloidal mixing method utilizing NMP was employed to disperse the CNTs into the AlSi10Mg powder. The dispersion process was detailed in our previous study [19]. Consequently, composite powders with uniformly dispersed CNTs were successfully obtained with a content no more than 2.0wt.%.

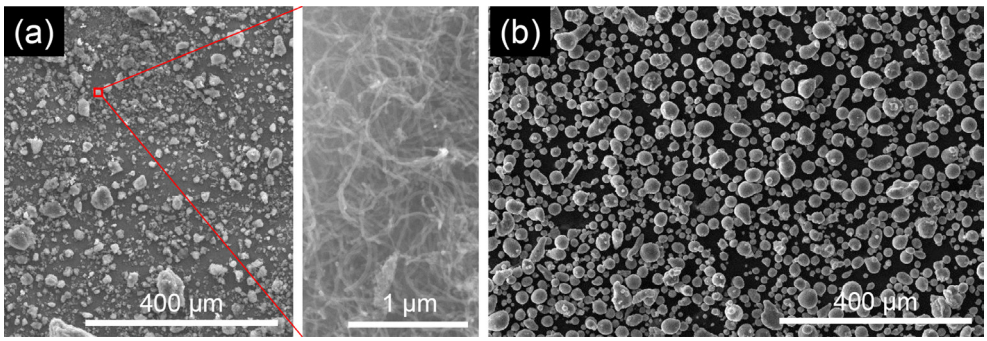

Fig. 1: Raw CNTs powder (a) and raw AlSi10Mg powder (b)

2.2 LPBF process

The Concept Laser M2 Cusing system (400 W, single laser) from Concept Laser GmbH Co., Ltd. was employed for the LPBF process of composite powders containing CNT fractions ranging from 0.0 to 2.0wt.% (0.0, 0.5, 1.0, 1.5, and 2.0, wt.%). Argon gas with a purity of 99.999% was used as the protective atmosphere. The LPBF parameters were set as follows: a laser power of 370 W, a scan spacing of 105 μm, a powder layer thickness of 30 μm, and scan speeds ranging from 900 to 1,900 mm·s^{-1} in intervals of 200 mm·s^{-1}. The default zigzag scan strategy was utilized during intra-layer scanning, with a 90° rotation implemented between adjacent layers. The fabricated samples for testing measured 10 mm×10 mm×10 mm.

2.3 Characterization

An Aramis Raman spectrometer (HORIBA Scientific Co., Ltd., France) was employed to evaluate the structural changes of CNTs in composite powders at a wavelength of 532 nm. The hardness of the samples, mechanically ground and polished in standard routines, was measured using a TMHV-50MD HV-50 micro-Vickers hardness tester (Shanghai Tu Ming Optical Instrument Co., Ltd., China). Microstructural analysis of the etched samples was conducted using an FEI Quanta 250F scanning electron microscope (SEM) with an Oxford energy dispersive spectrometer (EDS) at 30 kV and a Zeiss Auriga SEM equipped with an electron backscattered diffraction detector (EBSD) at 20 kV. Keller reagent (HF: HCl: HNO_3: H_2O = 1: 1.5: 2.5: 95) was used for etching the polished SEM samples. For EBSD analysis, samples were firstly mechanically polished, followed by electrochemical polishing in a solution of perchloric acid and ethanol (1: 9), applying a voltage of 20 V for 15 s at –20 °C. To analyze the morphology of CNTs in ion-milled samples, an FEI Tecnai G2 transmission electron microscope was utilized at 200 kV. A UMT-2EC friction and wear tester (Bruker Co., Ltd., Germany) was utilized to determine tribological properties of the samples at a scan speed of 1,300 mm·s^{-1}. A GCr15 bearing steel ball (63 HRC) with a diameter of 4 mm was used as the friction material. During dry friction testing, the relative sliding speed was set to 20 mm·s^{-1}, the normal load to 9 N, and the test duration to 30 min. The worn surfaces were examined using both a scanning electron microscope (SEM) and a laser scanning confocal microscope (LSCM) (Keyence VK-X150K, Japan).

3 Results

3.1 Morphology of mixed powders

The morphologies of the mixed powders with various CNT contents are shown in Fig. 2. The sphericity and size of the mixed powders [Figs. 2(a), (c), (e), (g), and (i)] are nearly consistent with those of the raw AlSi10Mg powder [Fig. 1(b)], which can be attributed to the effectiveness of the colloidal mixing process. It ensures acceptable powder bed behavior for LPBF [20]. At higher magnifications [Figs. 2(b), (d), (f), (h), and (j)], CNTs are found to be uniformly distributed on the powder surface until their content exceeds 2.0wt.%. As the CNT content increases, the density of CNT distribution on the powder surface also increases, with small agglomerations (submicron scale) appearing when the CNT content reached 1.5wt.% and 2.0wt.%, as indicated by the orange arrows in Figs. 2(f) and (h). When the

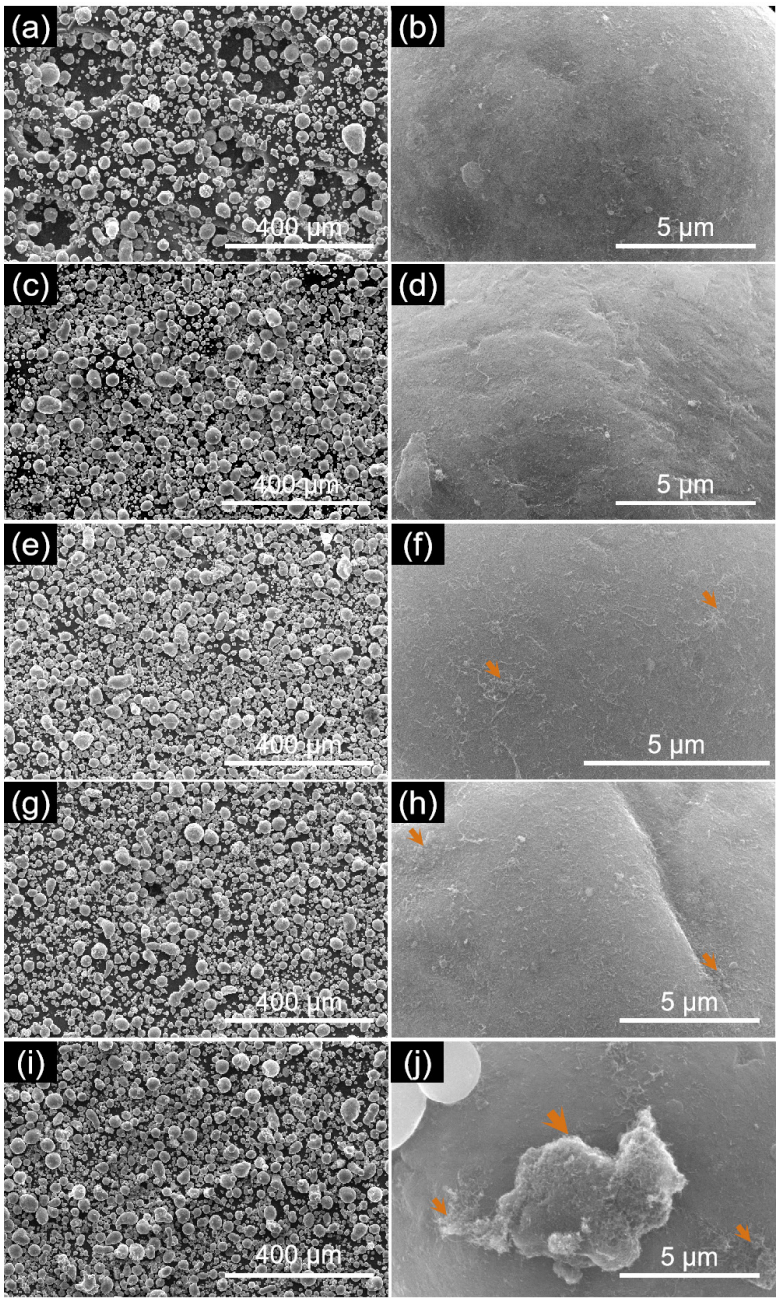

Fig. 2: Mixed powder with different CNT contents: (a) and (b) 0.5wt.%; (c) and (d) 1.0wt.%; (e) and (f) 1.5wt.%; (g) and (h) 2.0wt.%; (i) and (j) 3.0wt.%

CNT content reaches 3.0wt.%, the clusters in the powder surface become larger, with diameters of around 5 μm [Fig. 2(j)]. The primary reason is the limited surface area of the matrix powder, which results in agglomerations at higher CNT contents. Figure 2 shows that the maximum carbon nanotube content is 2.0wt.% to get homogeneous dispersion. Consequently, the discussion in this study primarily focused on the samples with a CNT content no more than 2.0wt.%.

Raman spectroscopy was commonly employed to investigate the structure and defects of carbon materials. According to the Raman shift of the mixed powders (Fig. 3), the ratio of the damage band (D-band) of CNTs at approximately 1,340 cm^{-1} to the graphite band (G-band) at around 1,570 cm^{-1} (I_D/I_G ratio) changes from 0.899 (raw CNTs) to 0.975 (mixed powder with 1.0wt.% CNTs) and 1.020 (mixed powder with 2.0wt.% CNTs) after colloidal mixing. This indicates that the structure of CNTs is well-preserved in the composite powders. In general, the colloidal mixing method demonstrates excellent dispersion performance for CNTs composite powders.

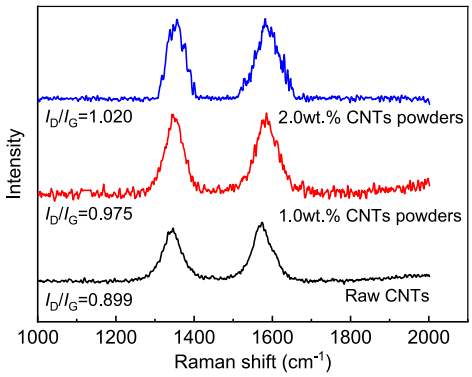

Fig. 3: Raman shift of raw CNTs and mixed powders

3.2 Microstructure of LPBF samples

According to the density and hardness results of all test samples (Fig. 7), the samples processed at a consistent scan speed of 1,300 $mm \cdot s^{-1}$ exhibits a balanced performance in terms of both density and hardness. The microstructures of these samples in the horizontal direction are displayed in Fig. 4 for later

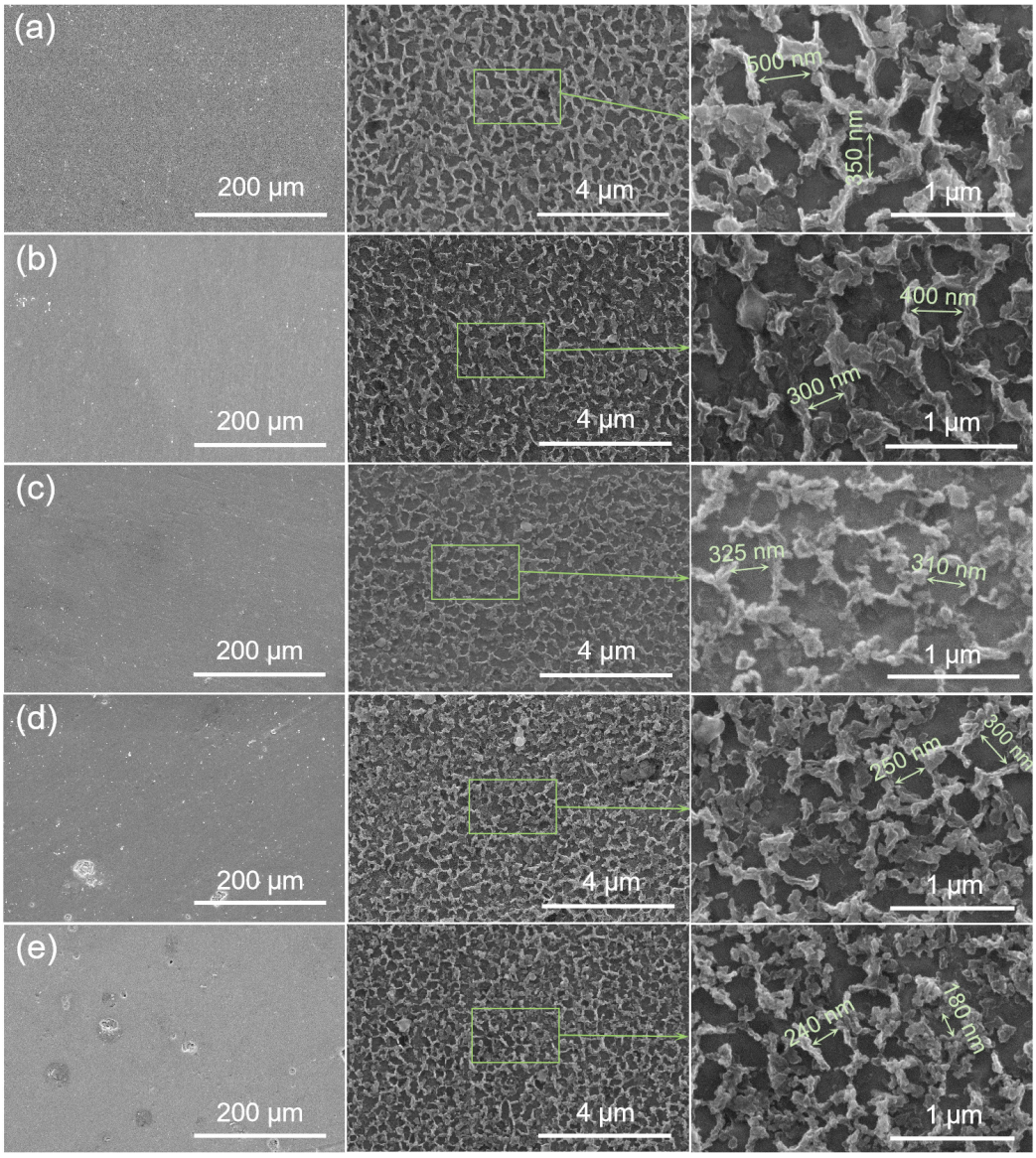

Fig. 4: Microstructures of the test samples with varying CNT contents at a scan speed of 1,300 $mm \cdot s^{-1}$, observed at different magnifications: (a) 0.0wt.%; (b) 0.5wt.%; (c) 1.0wt.%; (d) 1.5wt.%; (e) 2.0wt.%

discussion. At a low magnification (left column of Fig. 4), an increase in porosity is observed with higher CNT contents. At a high magnification of the fine zone (right column of Fig. 4), the network structure of the CNTs/AlSi10Mg composite resembles that of LPBFed AlSi10Mg. Furthermore, the microstructure exhibits a refining trend as CNT content increases, with the network size decreasing from approximately 500 nm to 200 nm.

A hierarchical microstructure consisting of coarse grains and ultrafine grains is shown in Fig. 5. Further EBSD statistical studies were conducted on the ultrafine grain regions for samples containing CNTs. As the CNT content increases, the size ratio of the ultrafine grain regions also increases. The EBSD results of the ultrafine grains regions [Figs. 5(b) and (c)] indicates that the grain size exhibits a refining trend with increasing CNT content. Furthermore, the grain size in the coarse regions also decreases significantly.

The morphologies of CNTs in the CNTs/AlSi10Mg samples with 1.0wt.% and 2.0wt.% CNTs are displayed in Fig. 6. As observed, the CNTs in both samples are uniformly distributed within the matrix, exhibiting random orientation at the cellular matrix. However, the length of the CNTs in the test samples

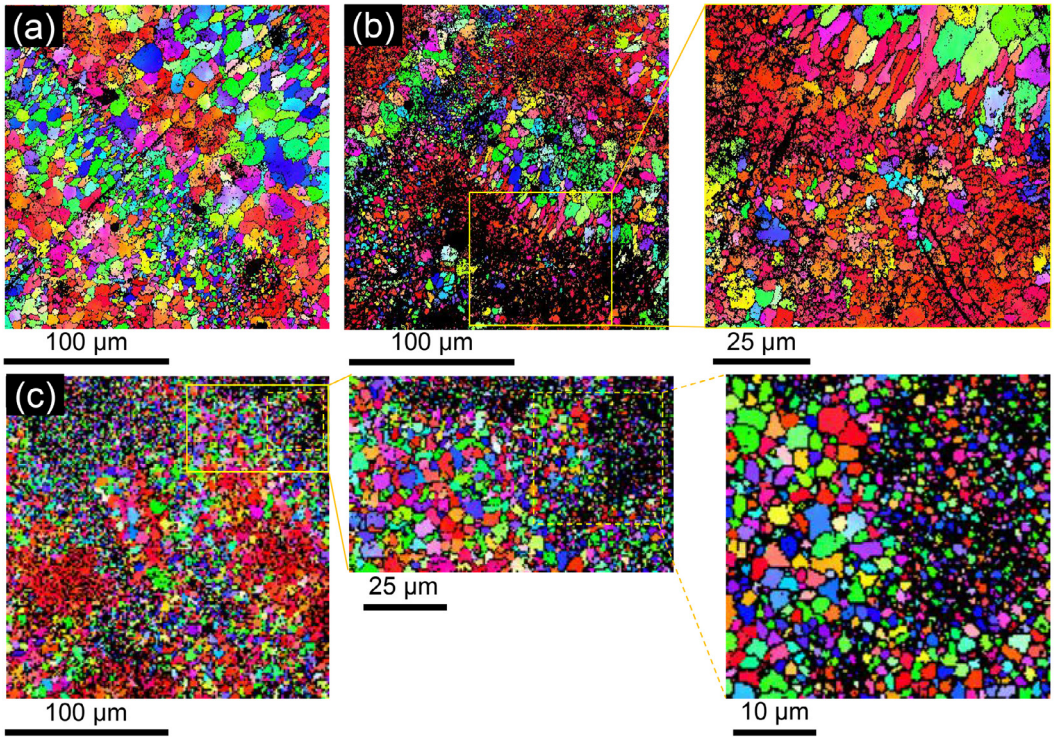

Fig. 5: EBSD results of the test samples with varying CNT contents at a scan speed of 1,300 mm·s^{-1}: (a) 0.0wt.%; (b) 1.0wt.%; (c) 2.0wt.%

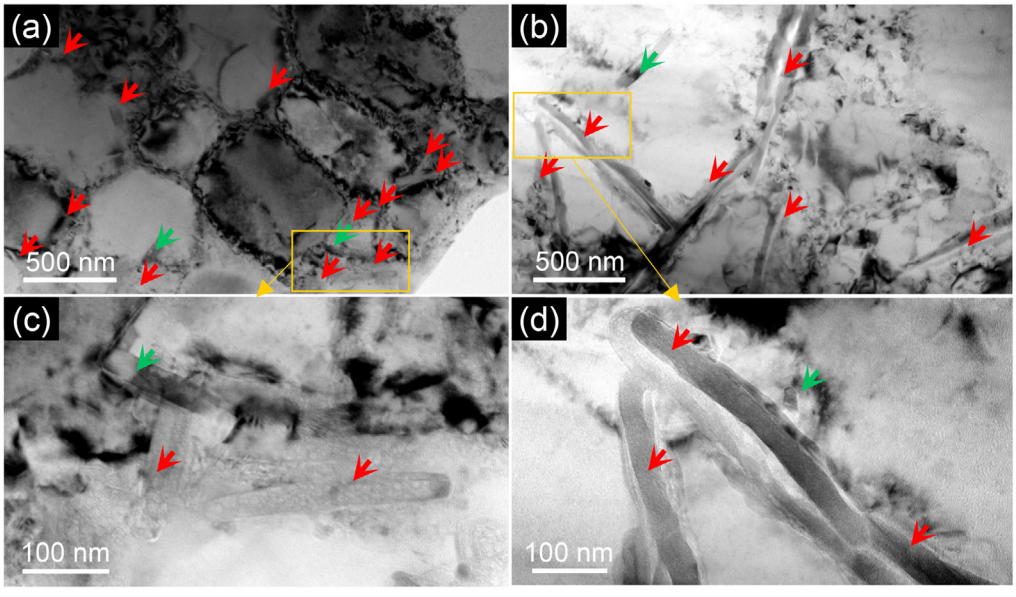

Fig. 6: TEM micrographs of the test samples with varying CNT fractions at a scan speed of 1,300 mm·s^{-1}: (a) and (c) 1.0wt.%; (b) and (d) 2.0wt.%

is shorter than that of the original CNTs [Fig. 1(a)]. The significant difference between the two samples lies in the morphology of the CNTs. In the samples with 1.0wt.% CNTs, the CNTs exhibit lengths of 200–300 nm [Fig. 6(c)], whereas in the samples with 2.0wt.% CNTs, the CNTs have lengths of 500–1,000 nm [Fig. 6(d)].

3.3 Relative density and hardness

As the scan speed increases from 900 to 1,900 mm·s^{-1}, the relative density of the LPBF samples with CNT contents ranging from 0.0wt.% to 1.5wt.% firstly increases and then decreases, while the relative density of the LPBF samples with 2.0wt.% CNT content continuously decreases [Fig. 7(a)]. When the CNT content reaches 2.0wt.%, the density of the LPBF samples drops significantly. The hardness of the LPBF samples reaches a maximum value of 143.3 HV when the CNT content is 1.0wt.% and the laser scan speed is 1,300 mm·s^{-1}. Correspondingly, test deviations increase with CNT content, as indicated by the error bars, due to the inconsistency of density and reinforcement. Increasing the density of the samples may further improve their mechanical performance.

3.4 Tribological properties

The CoF is a key factor of tribological property which indicates the amount of friction existing between two surfaces. The CoF curves [Fig. 8(a)] during the friction test exhibit substantial fluctuations in the first 600 s, indicating a running-in process between the composites and the friction material. After 600 s, the curves stabilize, entering a steady friction stage. The mean CoF [Fig. 8(b)] during this stable friction stage shows a decreasing trend with increasing CNT content. At a CNT content of 2.0wt.%, the composite achieves the lowest CoF of 0.37. However, the CoF of the sample with 1.5wt.% CNTs shows a slight increase compared to the sample with 1.0wt.% CNTs.

Wear rate is another key factor to evaluate the tribological properties of the test samples. Therefore, to further investigate the tribological properties of CNTs/AlSi10Mg, the wear rates [Fig. 8(b)] of the composites were additionally calculated using Eq. (1), as described in the work of Huang et al. [21]:

$$K=\frac{\Delta V}{F\cdot f\cdot A\cdot T}=\frac{\Delta V}{F\cdot v_f\cdot T} \quad (1)$$

where K is the wear rate, ΔV is the volume loss during the friction test directly measured by LSCM [Fig. 9(f)], F is the load force, f is the frequency, A is the amplitude, T is the sliding time, and v_f is the sliding speed. Figure 8(b) shows that the wear rate reaches the lowest value of 0.82×10^{-3} mm^3·Nm^{-1} at a CNT content of 2.0wt.%. Combining the experimental CoF results, the increased CNTs fraction effectively enhances the tribological properties of the composites, resulting in approximately 14% and 30% improvements in CoF and wear rate, respectively.

4 Discussion

4.1 Microstructure formation mechanism of CNTs/AlSi10Mg composites by LPBF

The Al-C reaction occurs readily when the temperature exceeds 500 °C. Given that the laser scanning track by track induces heating and cooling cycles, the Al-C reaction is facilitated during the LPBF process. Consequently, Al-C is detected in samples with varying CNT contents. Zhou et al. [22] investigated the interface and interfacial reactions between CNTs and Al,

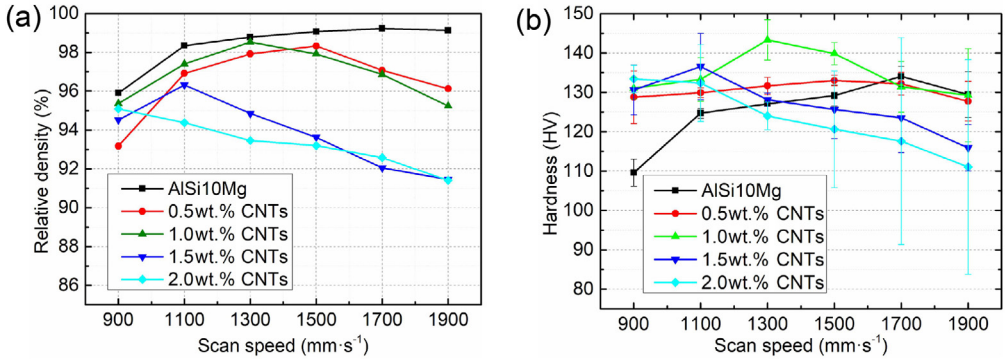

Fig. 7: Relative density (a) and hardness (b) of test samples with varying CNT fractions at different scan speeds

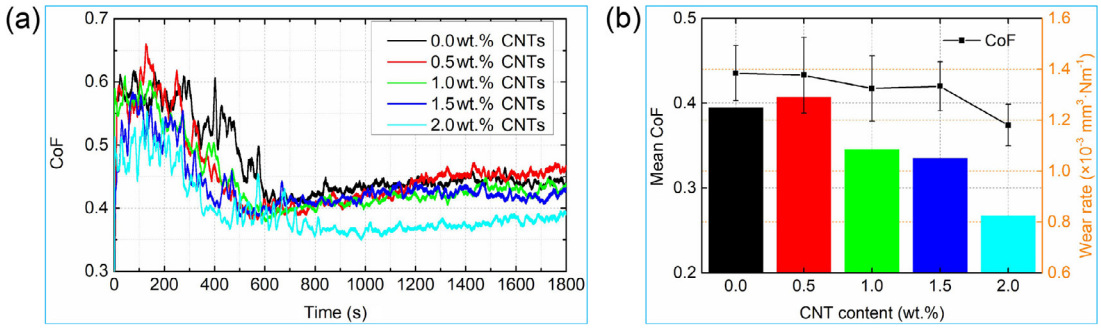

Fig. 8: Friction test results: (a) CoF curves of test parts vs. friction time; (b) mean CoF and wear rate vs. CNT content

discovering that Al-C preferentially forms at the active prism plane edges located at the open ends of the CNTs. Further research by Zhou et al. [23] indicated that the C atoms at the ends of CNTs exhibit higher activity due to the presence of more edges, vacancies, and dangling bonds. These C atoms more readily diffuse for a $C+Al \rightarrow Al_4C_3$ reaction within the high-temperature molten pool during LPBF. This reaction likely results in shorter CNTs lengths in the LPBF samples compared to the original materials. Moreover, it is assumed that the amount of CNTs consumed by the reaction remains constant under the same laser input energy density. Therefore, as the initial CNT content in the powders increases, a larger number of CNTs survive in the specimens. Samples with 2.0wt.% CNTs exhibit relatively more intact structures and denser distributions [Fig. 6(b)]. Additionally, Yuan and Chen [24] noted that direct laser irradiation can also shorten the size of CNTs. However, a significant portion of the powder surface is not directly exposed to the laser beam during the LPBF process. Direct laser irradiation leads to variations in CNTs lengths (Fig. 6) not only among samples with different CNT contents but also within the same sample. Consequently, the primary mechanism leading to the reduction in CNTs length is the reaction between Al and CNTs.

Kou [25] found that the morphology and size of solidification structures are related to the temperature gradient G and the growth rate R. The ratio G/R determines the morphology of the solidification structure, while the product $G \cdot R$ determines the size of the solidification structure. In AlSi10Mg, cellular dendrites are the primary solidification structures. Takata et al. [26] discovered that supersaturated Si was contained in α-Al in as-built AlSi10Mg. During the solidification process, the Si remaining in the molten pool precipitates around the growing cellular Al dendrites. Due to poor wettability between CNTs and molten Al, the CNTs are excluded from the grains and solidify within the liquid film between the cellular dendrites. As a result, the CNTs end up co-located with Si. Surappa [27] indicated that the presence of reinforcement affects the grain size of the matrix by restricting grain growth. The uniformly distributed CNTs at the cellular matrix provide resistance to the growth of cellular dendrites in molten pool. Therefore, CNTs surrounding the cellular dendrites effectively restrain grain growth and contribute to the formation of a more complete Si network.

Although the addition of CNTs reduces the size of cellular dendrites and completes the network structure, it unfortunately increases porosity. The large surface area of CNTs makes the material highly absorptive of H_2O and gas. Consequently, as more CNTs are added, more gas is incorporated into the composite powders, leading to more evaporation pores in the LPBF samples. Additionally, a previous study found that good metallurgical bonding between adjacent scan lines and reduced internal porosity could be achieved at a scan speed of 1,300 $mm \cdot s^{-1}$ with 1.0wt.% CNTs during the LPBF process [17]. Gu et al. [28] discovered that the viscosity of the molten pool increases with a higher reinforcement content, which reduces the flowability of the melt. Therefore, more energy is required to spread the molten pool as the CNT content increases. Consequently, higher porosity is observed in composites with increased CNT content [Figs. 4(d) and (e), and Fig. 7(a)] when using the same laser parameters.

4.2 Strengthen mechanism of CNTs

Huang et al. [29] discovered that a net-like microstructure, where a hard phase encapsulated a soft phase to form an inhomogeneous architecture, aligns with the upper bound of the Hashin-Shtrikman theory. In the research of Li et al. [30], higher mechanical properties compared to cast and aged AlSi10Mg samples are attributed to a nearly continuous reticulated silicon structure in the microstructure of LPBF AlSi10Mg samples. The enhanced completeness and continuity of the microstructure due to CNTs contributed to improved composite hardness. Additionally, the Hall-Petch effect, resulting from grain size refinement induced by CNTs, also contribute to the improvement of composite's performance. Chen et al. [31] found that dislocations could be impeded due to Orowan strengthening induced by CNTs with an aspect ratio of approximately 10. Overall, the hardness of the LPBF samples is enhanced by these three mechanisms with the addition of CNTs. However, when CNT content exceeds 1.0wt.%, increased porosity [Fig. 7(a)] begins to diminish these strengthening effects. Consequently, the maximum hardness of composites with 1.5wt.% and 2.0wt.% CNTs is lower than that of the composite with 1.0wt.% CNTs.

Moreover, the test results [Fig. 7(b)] indicate that the scan speed corresponding to peak relative density decreases as the CNT content increases. Hence, the peak hardness of the test samples decreases. According to the equation of laser energy density [32, 33] in Eq. (2), the input energy density increases as the scan speed decreases.

$$\eta = P/v \tag{2}$$

where η represents the laser energy density, P denotes the laser power, and v is the scan speed. Increasing the input energy by reducing the scan speed aids in the spreading of the molten pool and enhances bonding between scan tracks. Consequently, the optimal scan speed for CNTs/AlSi10Mg composites decreases as the CNT content increases.

4.3 Fiction behavior and wear mechanism

Grooves are observed on the worn surfaces of all samples (Fig. 9). The primary difference among the worn surfaces is the depth of these grooves. Generally, the groove depth decreases with increasing CNT content, except for the sample shown in Fig. 9(b). This observation aligns with the wear rate results.

The SEM images of the worn surfaces (Fig. 10) reveal the presence of grooves and an adhesive tribolayer. Consequently, the primary wear mechanisms during the friction test are identified as abrasive wear and adhesive wear.

In samples with a higher CNT content, the adhesive tribolayer area is reduced and the grooves are less pronounced. According to Archard's theory [34], shearing of junctions under applied force leads to deformation in the subsurface region of a softer material, resulting in the formation of microcracks.

Consequently, wear debris and the adhesive tribolayer form as the deformed material detaches from the softer specimen's surface. Additionally, the EDS analysis of the vertical-cross section of worn sample with 2.0wt.% CNTs reveals that Al, C, and Si are the predominant elements present on the worn surface (Fig. 11). During the friction test, these elements on the worn sufarce are generally accompanied by relative oxides. Unfortunately, the oxides act as third-body abrasives, exacerbating surface wear. This phenomenon aligns with the investigation of Kang et al. [35], who found that silicon oxides and aluminum oxides were primarily caused by oxidation reactions. However, the chemical reaction leading to these oxides could not be mitigated by the addition of CNTs.

With the addition of CNTs, the network microstructure becomes more stable due to the hybrid strengthening effect of CNTs and Si. As a result, adhesive wear is reduced on the worn surfaces. Additionally, Zhai et al. [36] discovered that CNTs can form a self-lubricating film, preventing direct contact between sliding surfaces. This can be found in Fig. 11(c) in this study. These self-lubricating films minimize the ploughing effect of hard asperities, as the carbon film reacts with oxygen more readily than Al and Si during friction.

Overall, the wear resistance is enhanced through two primary mechanisms: reduced adhesive wear area and shallower grooves. Higher CNT contents contribute to a lower CoF and wear rate in the composites. However, based on the analysis of CNT morphology in LPBF samples, if the amount of CNTs is insufficient, they are almost entirely reacted, which can diminish the composite's wear resistance, as observed in samples with 0.5wt.% CNTs [Fig. 9(b)]. Additionally, Baradeswaran and Perumal [37] found that pores in the samples increase the CoF and wear rate of the composites due to the large bearing area and stress concentration around the pores. Consequently, the presence of pores in the LPBF samples, such as observed in the worn surface of the sample with 1.5wt.% CNTs [indicated by the blue circle in Fig. 10(d)], is believed to have resulted in relatively lower tribological performance for these samples with CNT content exceeding 1.0wt.%.

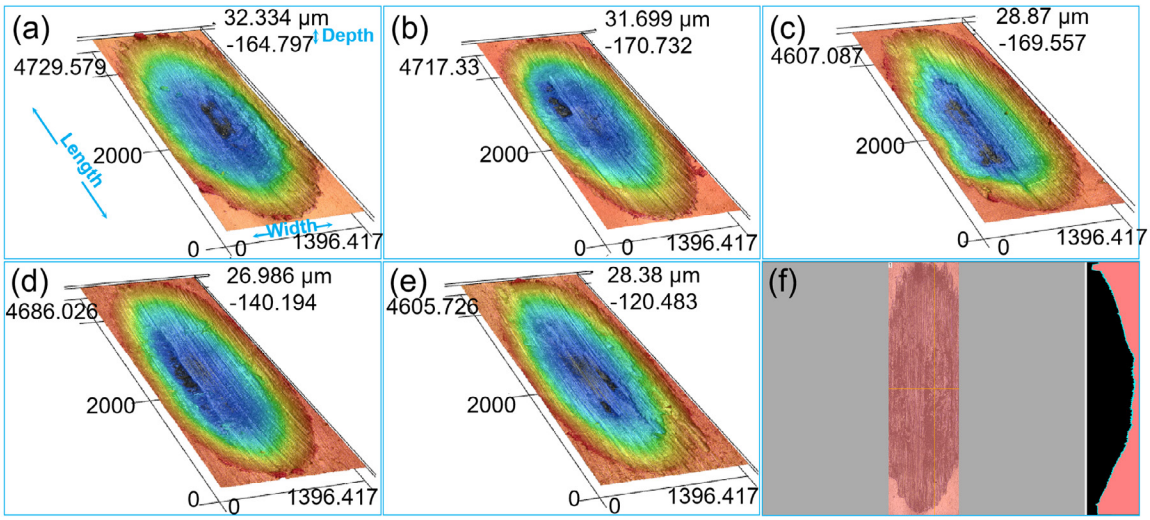

Fig. 9: Complete morphology of worn surfaces at varying CNT contents as observed through LSCM: (a) 0.0wt.%; (b) 0.5wt.%; (c) 1.0wt.%; (d) 1.5wt.%; (e) 2.0wt.%; (f) volume measure process

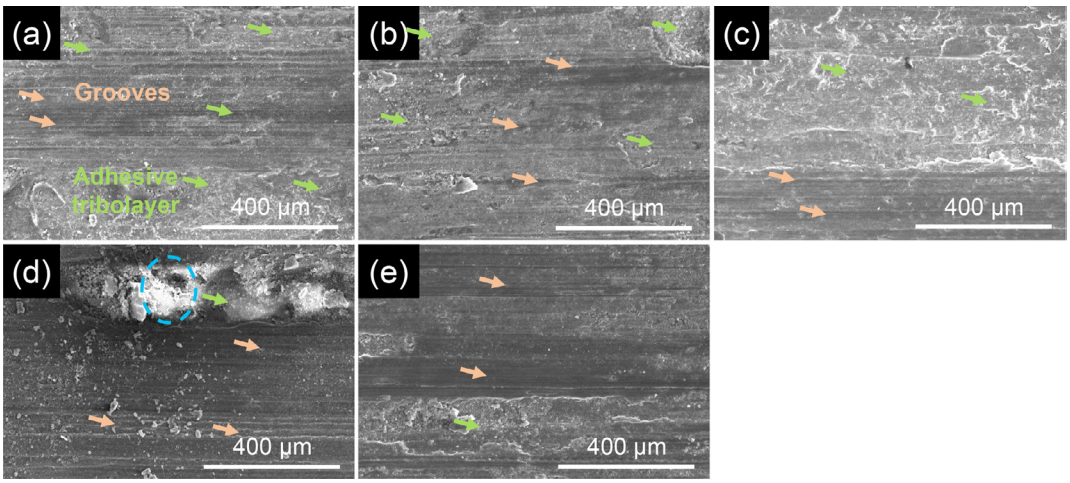

Fig. 10: Morphology of worn surfaces of CNTs/AlSi10Mg composite samples with varying CNT contents observed via SEM: (a) 0.0wt.%; (b) 0.5wt.%; (c) 1.0wt.%; (d) 1.5wt.%; (e) 2.0wt.%. The area of adhesive tribolayer is marked in green arrows and the area of grooves is marked in orange arrows

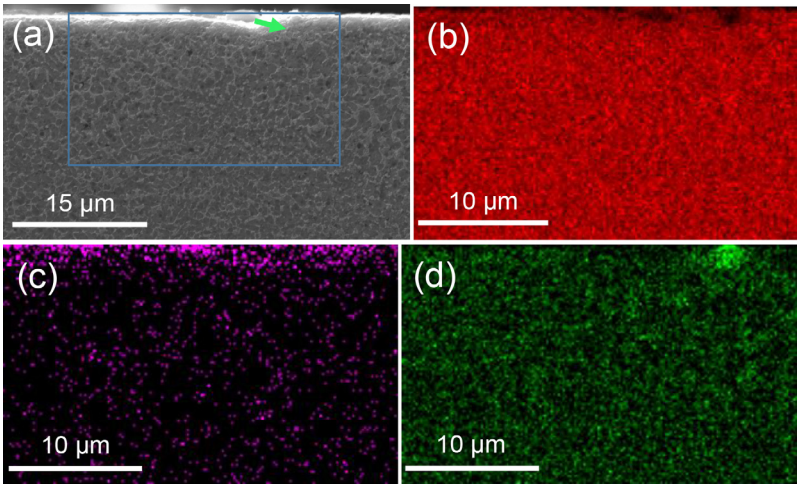

Fig. 11: Element distribution in the vertical cross-section of worn sample with 2.0wt.% CNTs: (a) SEM; (b) Al; (c) C; and (d) Si

In summary, the addition of CNTs improves the tribological properties of the matrix. However, this enhancement is not significant when the CNT content is insufficient, as some CNTs are consumed by the reactions. Furthermore, the presence of pores in the LPBF samples adversely affects the tribological properties of CNTs/AlSi10Mg composites. As a result, the best performance of the composites is achieved when the CNT content is 1.0wt.%.

5 Conclusions

In this study, the impact of carbon nanotube (CNT) content on the hardness and tribological properties of CNTs/AlSi10Mg composites fabricated by laser powder bed fusion was investigated. The following conclusions are drawn:

(1) Uniform distribution of CNTs can be achieved through a colloidal mixing method. However, when CNT content exceeds 2.0wt.%, agglomerations become more pronounced due to the limited surface area of the matrix powder. As a result, the maximum CNT content for achieving homogeneous dispersion in composite powders is 2.0wt.%.

(2) In CNTs/AlSi10Mg, CNTs are primarily distributed along the cellular matrix boundaries, with some reacting to form aluminum carbides. As the CNT content increases, a more complete CNT structure persists in the LPBF samples, resulting in a finer and more continuous microstructure. The length of CNTs in composites containing 1.0wt.% CNTs is approximately 200–300 nm, while in composites with 2.0wt.% CNTs, it ranges approximately 500–1,000 nm. The main mechanism for the shortening of CNTs is their reaction with aluminum.

(3) The hardness of the samples reaches its highest value, 143.3 HV, when the CNT content is 1.0wt.% and the scan speed is 1,300 $mm \cdot s^{-1}$. The primary strengthening mechanisms contributing to the improvement in hardness are the pinning effect, the Orowan mechanism, and the Hall-Petch effect. However, when the CNT content exceeds 1.0wt.%, the increase in porosity has a greater effect than the strengthening provided by the CNTs, leading to a decrease in hardness. Moreover, the optimal scan speed for CNTs/AlSi10Mg composites decreases as the CNT content increases, while other parameters remain constant.

(4) The wear mechanisms observed in the samples are adhesive wear and abrasive wear. Material damage during the friction process is reduced as the CNT content increases. The coefficient of friction (CoF) of the samples decreases with increasing CNT content. At a CNT content of 2.0wt.%, the CoF and wear rate decrease to 0.37 and 0.82×10^{-3} $mm^3 \cdot Nm^{-1}$, respectively, which are approximately 14% and 30% lower than those of the unreinforced matrix. The self-lubricating properties of the CNTs significantly contribute to the improved friction performance.

Acknowledgments

This study was supported by the Natural Science Foundation of Jiangsu Higher Education Institutions of China (Grant No. 23KJD460003), the Scientific Research Foundation for High-level Talents of Nanjing Institute of Technology (Grant No. YKJ202103), and the National Natural Science Foundation of China (Grant Nos. 92463301, 92163215, 52205471, 52305470). We greatly appreciate the valuable discussion on tribological characteristics with Dr. Chao Li. Special thanks to Ms. Li-hua Xie for her assistance in the post-processing of the LPBF samples.

Conflict of interest

We declare that we have no financial or personal relationships with other individuals or organizations that could inappropriately influence our work. There are no professional or personal interests of any nature or kind in any product, service, and/or company that could be construed as influencing the position presented in, or the review of, the manuscript entitled “Effect of CNT content on microstructure and tribological properties of CNTs/AlSi10Mg composites by LPBF”.

References

[1] Amirkhanlou S, Ji S X. Casting lightweight stiff aluminum alloys: A review. Critical Reviews in Solid State and Materials Sciences, 2020, 45(3): 171–186.
[2] Fan Z Z, Yuan W Q, Wang D Z, et al. Research status and future development trend of die casting aluminum alloys. Foundry, 2020, 69(2): 159–166. (In Chinese)
[3] Mistry J M, Gohil P P. An overview of diversified reinforcement on aluminum metal matrix composites: Tribological aspects. Proceedings of the Institution of Mechanical Engineers–Part J, 2017, 231(3): 399–421.
[4] Valizade N, Farhat Z. A review on abrasive wear of aluminum composites: Mechanisms and influencing factors. Journal of Composites Science, 2024, 8(4): 149.
[5] Li Z, Zhang D. The self-stimulation effect for high-performance metal matrix composites. Materials China, 2023, 42(8): 605–613. (In Chinese)
[6] Bharat N, Bose P S. An overview of production technologies and its application of metal matrix composites. Advances in Materials and Processing Technologies, 2022: 8(2): 1946–1962.
[7] Zhang Z L, Xiao Y, Xu J, et al. Microstructure characteristics and thermodynamic properties of A357-SiC_p/A357 layered composites prepared by semi-solid vacuum stirring suction casting. China Foundry, 2023, 20(2): 108–114.
[8] Xiao Z, Yu W H, Fu H X, et al. Recent progress on microstructure manipulation of aluminium alloys manufactured via laser powder bed fusion. Virtual and Physical Prototyping, 2022, 18(1): e2125880.
[9] Yu W H, Sing S L, Chua C K, et al. Particle-reinforced metal matrix nanocomposites fabricated by selective laser melting: A state of the art review. Progress in Materials Science, 2019, 104: 330–379.
[10] Jue J, Gu D. Selective laser melting additive manufacturing of in situ $Al_2Si_4O_{10}$/Al composites: Microstructural characteristics and mechanical properties. Journal of Composite Materials, 2016, 51: 519–532.
[11] Gao C, Wang Z, Xiao Z, et al. Selective laser melting of TiN nanoparticle-reinforced AlSi10Mg composite: Microstructural, interfacial, and mechanical properties. Journal of Materials Processing Technology, 2020, 281: 116618.
[12] Xu T Y, Zhu Z W, Mi G Y, et al. Revealing the mechanism of laser welded aluminum alloy joints in-situ reinforced by carbon nanotubes based on microstructural evolution. Materials Characterization, 2022, 193: 112327.
[13] Zhao X, Song B, Fan W R, et al. Selective laser melting of carbon/AlSi10Mg composites: Microstructure, mechanical and electronical properties. Journal of Alloys and Compounds, 2016, 665: 271–281.
[14] Du Z, Tan M J, Guo J F, et al. Aluminium-carbon nanotubes composites produced from friction stir processing and selective laser melting. Materials Science & Engineering Technology, 2016, 47(5–6): 539–548.
[15] Wang L Z, Chen T, Wang S. Microstructural characteristics and mechanical properties of carbon nanotube reinforced AlSi10Mg composites fabricated by selective laser melting. Optik, 2017, 143: 173–179.
[16] Gu D D, Rao X W, Dai D H, et al. Laser additive manufacturing of carbon nanotubes (CNTs) reinforced aluminum matrix nanocomposites: Processing optimization, microstructure evolution and mechanical properties. Additive Manufacturing, 2019, 29: 100801.
[17] Jiang L Y, Liu T T, Zhang C D, et al. Preparation and mechanical properties of CNTs-AlSi10Mg composite fabricated via selective laser melting. Materials Science and Engineering: A, 2018, 734: 171–177.
[18] Azar N S, Pourfath M. Aggregation kinetics and stability mechanisms of pristine and oxidized nanocarbons in polar solvents. The Journal of Physical Chemistry: C, 2016 120: 16804–16814.
[19] Jiang L Y, Liu T T, Zhang C D, et al. Thermal expansion behavior of CNT reinforced AlSi10Mg composite fabricated via laser powder bed fusion. Materials Research Express, 2020, 6: 125806.
[20] Mussatto A, Groarke R, O'Neill A, et al. Influences of powder morphology and spreading parameters on the powder bed topography uniformity in powder bed fusion metal additive manufacturing. Additive Manufacturing, 2021, 38: 101807.
[21] Huang L, Yuan J T, Li C. Influence of titanium concentration on mechanical properties and wear resistance to Ti6Al4V of Ti-C:H on cemented carbide. Vacuum, 2017, 138: 1–7.
[22] Zhou W W, Bang S, Kurita H, et al. Interface and interfacial reactions in multi-walled carbon nanotube-reinforced aluminum matrix composites. Carbon, 2016, 96: 19–928.
[23] Zhou W W, Dong M Q, Zhou Z X, et al. In situ formation of uniformly dispersed Al_4C_3 nanorods during additive manufacturing of graphene oxide/Al mixed powders. Carbon, 2019, 141: 67–75.
[24] Yuan Y P, Chen J M. Morphology adjustments of multi-walled carbon nanotubes by laser irradiation. Laser Physics Letters, 2016, 13(6): 066001.
[25] Kou S. Welding Metallurgy, Second Edition, Hoboken: Wiley Online Books, 2003: 70–198.
[26] Takata N, Kodaira H, Sekizawa K, et al. Change in microstructure of selectively laser melted AlSi10Mg alloy with heat treatments. Materials Science and Engineering: A, 2017, 704: 218–228.
[27] Surappa M K. Microstructure evolution during solidification of DRMMCs (discontinuously reinforced metal matrix composites): State of art. Journal of Materials Processing Technology, 1997, 63: 325–333.
[28] Gu D D, Chang F, Dai D H. Selective laser melting additive manufacturing of novel aluminum based composites with multiple reinforcing phases. Journal of Manufacturing Science and Engineering, 2015, 137(2): 021010.
[29] Huang L J, Geng L, Peng H X. Microstructurally inhomogeneous composites: Is a homogeneous reinforcement distribution optimal? Progress in Materials Science, 2015, 71: 93–168.
[30] Li X P, Ji G, Chen Z, et al. Selective laser melting of nano-TiB_2 decorated AlSi10Mg alloy with high fracture strength and ductility. Acta Materialia, 2017, 129: 183–193.
[31] Chen B, Shen J, Ye X, et al. Length effect of carbon nanotubes on the strengthening mechanisms in metal matrix composites. Acta Materialia, 2017, 140: 317–325.
[32] Gu D D, Shen Y F. Effects of processing parameters on consolidation and microstructure of W-Cu components by DMLS. Journal of Alloys and Compounds, 2009, 473: 107–115.
[33] Niu H J, Chang I T H. Selective laser sintering of gas atomized M2 high speed steel powder. Journal of Materials Science, 2000, 35: 31–38.
[34] Archard J F. Contact and rubbing of flat surfaces. Journal of Applied Physics, 1953, 24: 981–988.
[35] Kang N, Coddet P, Liao H L, et al. Wear behavior and microstructure of hypereutectic Al-Si alloys prepared by selective laser melting. Applied Surface Science, 2016, 378: 142–149.
[36] Zhai W Z, Srikanth N, Kong L B, et al. Carbon nanomaterials in tribology. Carbon, 2017, 119: 150–171.
[37] Baradeswaran A, Perumal A E. Wear and mechanical characteristics of Al 7075/graphite composites. Composites Part B: Engineering, 2014, 56: 472–476.